

Highly Selective Low-Temperature Acetylene Semihydrogenation Guided by Multiscale Machine Learning

Lin Chen, Xiao-Tian Li, Sicong Ma, Yi-Fan Hu, Cheng Shang, and Zhi-Pan Liu*



Cite This: *ACS Catal.* 2022, 12, 14872–14881



Read Online

ACCESS |



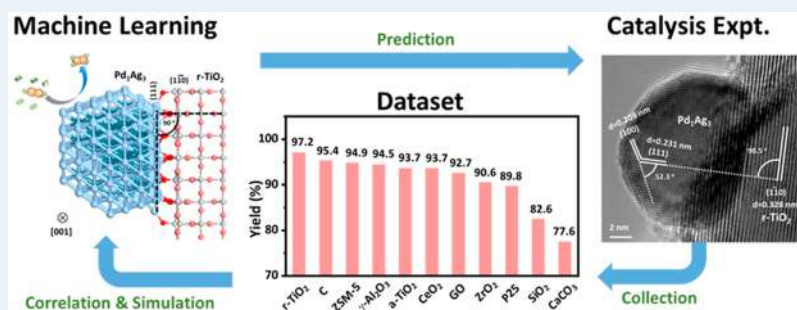
Metrics & More



Article Recommendations



Supporting Information



ABSTRACT: Catalytic hydrogenation is the key measure to remove traces of acetylene in ethylene in the petroleum industry. Herein we report a highly selective and stable nanocatalyst, Pd₁Ag₃ supported on rutile-TiO₂ (r-TiO₂) annealed at unusually high temperatures (>750 °C), which can purify ethylene mixed with 1% of acetylene at 97.2% selectivity and 100% acetylene conversion below 100 °C. The selectivity is more than 10% higher than that in our previous work. This advance is achieved by a rational catalyst search featuring machine learning to correlate catalyst synthesis conditions with the catalyst performance and a large-scale machine-learning atomic simulation for disclosing composite atomic structures at high temperatures. We show that Pd₁Ag₃ alloy crystal nanoparticles form until 727 °C and the alloy nanoparticles grow epitaxially on r-TiO₂(110) via its {111} facets. The maximum exposure of the alloy {111} surface is the key to the highest selectivity among the different supports tested, as confirmed by high-resolution characterization experiments and microkinetics simulations. Our results demonstrate the power of multiscale machine-learning tools in guiding the catalyst design and clarifying the atomic nature in complex heterogeneous catalysis.

KEYWORDS: acetylene hydrogenation, Pd₁Ag₃, r-TiO₂, machine learning simulation, random forest, SSW-NN

1. INTRODUCTION

The selective hydrogenation of acetylene to ethylene (semihydrogenation) in an excess of ethylene is one of the most important petrochemical processes used for purifying ethylene, a platform molecule with massive production.^{1–7} The industrial PdAg alloy catalyst, although utilized for years, does not have satisfactory activity and selectivity, typically obtaining ~55% selectivity at 90% acetylene conversion.^{8–14} How to effectively remove acetylene while avoiding undesired ethylene hydrogenation and oligomerization has been an intriguing but challenging problem in the industry for decades.^{15–19} Tremendous efforts have been devoted to searching for better catalysts, typically by replacing Pd or Ag with other elements, but little progress has been made in the performance under industrial conditions (low temperature, low acetylene:ethylene composition ratio).^{8,20–31} Herein with machine-learning (ML)-guided catalysis experiments we reveal a high-temperature annealed Pd₁Ag₃ alloy crystal catalyst supported on r-TiO₂, which achieves 97.2% selectivity at 100% acetylene conversion below 100 °C with an acetylene:ethylene ratio of 1:100.

The utilization of PdAg alloy as the industrial catalyst was long attributed to the essentiality of Pd for low-temperature hydrogenation and Ag alloying to block the low-selectivity sites.^{16,17} For pure Pd metal, despite its high activity as a hydrogenation catalyst, it transforms readily to PdH_x hydride phases under hydrogenation conditions, which promotes ethylene hydrogenation and thus reduces the selectivity.^{16,32–34} While the addition of Ag does prevent the formation of hydride phases, the active structure of the PdAg alloy during catalysis is largely elusive, since a face-centered-cubic (fcc) solid solution (random Pd–Ag distribution) was found when annealing below ~900 °C.³⁵ Fundamentally, this is due to the fact that the ordered PdAg alloy crystal is not strongly preferred thermodynamically compared to Pd and Ag

Received: September 5, 2022

Revised: October 19, 2022

metals: as confirmed by density functional theory (DFT) calculations,³⁶ Pd₁Ag₁, being the most stable alloy crystal phase, is only 0.06 eV/atom more stable than individual pure metals. Indeed, experiments have observed a dynamic Pd–Ag exchange on the surface of PdAg alloy above 447 °C, which suggests complex and heterogeneous surface structures for PdAg catalysts.^{37,38}

To correlate the catalytic selectivity with the catalyst active sites, we recently explored the acetylene hydrogenation pathways on a series of thermodynamically stable PdAg surface sites by using ML atomic simulations.³⁶ It was found that the Pd sites exposed on the {100} facets have the poorest selectivity and if {100} facet is blocked, for example, at Pd:Ag < 1:3 where the {100} facet is terminated by a full monolayer of Ag atoms under the reaction conditions, the selectivity can be boosted. These atomic-level understandings led to the finding of a r-TiO₂-supported Pd₁Ag₃ catalyst that can achieve ~85% selectivity at >96% acetylene conversion below 100 °C, after screening the Pd₁Ag₃ catalyst on a series of support materials.³⁶ Although the experimental results confirm the importance of the Pd:Ag ratio, the type of support material emerges as a new variable to influence the catalyst performance, which raises naturally the query on important variables possibly overlooked in the experiment for further improving the selectivity.

Here we utilize a multiscale ML-guided catalyst design approach to search the synthetic space to maximize the catalyst performance. As shown in Figure 1, a phenomenological-level ML³⁹ is first utilized to rank the importance of synthetic conditions from the experimental data set with a large variable

space, large-scale atomic simulations using global neural network potential⁴⁰ are then performed to reveal the catalyst structure evolution, and finally the designed catalysis experiments on key variables are carried out to validate the catalytic performance. By carefully tuning the annealing temperature and the supporting material (the factors ranked high by the ML model) in catalyst synthesis, using atomic simulations to observe PdAg growth dynamics, and performing detailed catalyst characterizations, we now manage to improve the acetylene semihydrogenation conversion and selectivity to 100% and 97.2% for the acetylene semihydrogenation. We show that this combinatorial approach effectively identifies the key parameters in synthesis and leads to a composite catalyst with high activity and selectivity for acetylene hydrogenation.

2. EXPERIMENTAL SECTION

2.1. Synthesis of Rutile-TiO₂. r-TiO₂ nanorods were synthesized using the procedure reported in the literature.⁴¹ Briefly, 6.6 mL of TiCl₄ was dissolved in 13.4 mL of distilled water within an ice–water bath to obtain a 3 M TiCl₄ solution. Then, 35 mL of concentrated nitric acid (68%, HNO₃) was refluxed at 140 °C, and then 20 mL of the 3 M TiCl₄ solution was quickly injected into vigorously stirred nitric acid solution. After 24 h of reaction, the final products were filtered, washed with distilled water, and then freeze-dried under vacuum.

2.2. Synthesis of PdAg/r-TiO₂. The PdAg catalysts were typically synthesized by a coimpregnation method and supported on r-TiO₂. Briefly, the r-TiO₂ was dispersed in an appropriate amount of water in a bottle. After sonication for 10 min and stirring for 30 min, the precursor (Pd(NO₃)₂·2H₂O and AgNO₃ solution) was added quickly to the mixture and stirring was continued for 12 h. Thereafter, the samples were freeze-dried under vacuum. Finally, after calcination in several gases (5% H₂/Ar, 100% H₂, N₂, air, and vacuum) at different annealing temperatures (150, 300, 450, 600, 750, and 900 °C) for a period, the PdAg/r-TiO₂ catalysts were obtained (see Figure 1b). For comparison, some samples were not calcined but reduced in solvent using chemical reagents (NaBH₄, DMAB, LiAlH₄, CO, etc.). Then, the products were collected and freeze-dried under vacuum. More details can be found in Section 1 in the Supporting Information.

2.3. Synthesis of PdAg with Other Supports. A range of different commercially available supports (anatase-TiO₂ (a-TiO₂), P25, ZSM-5, γ-Al₂O₃, α-Al₂O₃, CeO₂, ZrO₂, SiO₂, SnO₂, Y₂O₃, HT, CaCO₃, GO, C, MCM-41, Al-MCM-41, Ti-MWW, Ti-MOR, SAPO-34) were also examined as the PdAg catalyst supports. They were generally synthesized by a coimpregnation method, similar to the Pd₁Ag₃/r-TiO₂ catalysts. More details are summarized in Table S1.

2.4. Catalytic Hydrogenation Reactions. All catalytic reactions were performed in a continuous-flow fixed-bed microreactor. For comparison, all samples contain 0.25 mg of Pd, mixed with 20 g of green silicon carbide. The gas consists of 0.5% C₂H₂, 50.0% C₂H₄, 5.0% H₂, 4.0% He, and 40.5% N₂, fed at a flow rate of 40 mL/min. Prior to the reaction, the catalysts were pretreated in 5% H₂/Ar at 150 °C for 3 h and then cooled to the reaction temperature. The products were analyzed by an online gas chromatograph (GC, Agilent 7890B) equipped with two thermal conductivity detectors (TCDs) and a flame ionization detector (FID). The activity and selectivity of the catalysts were taken from the steady data after 6 h in the stream. The acetylene conversion,

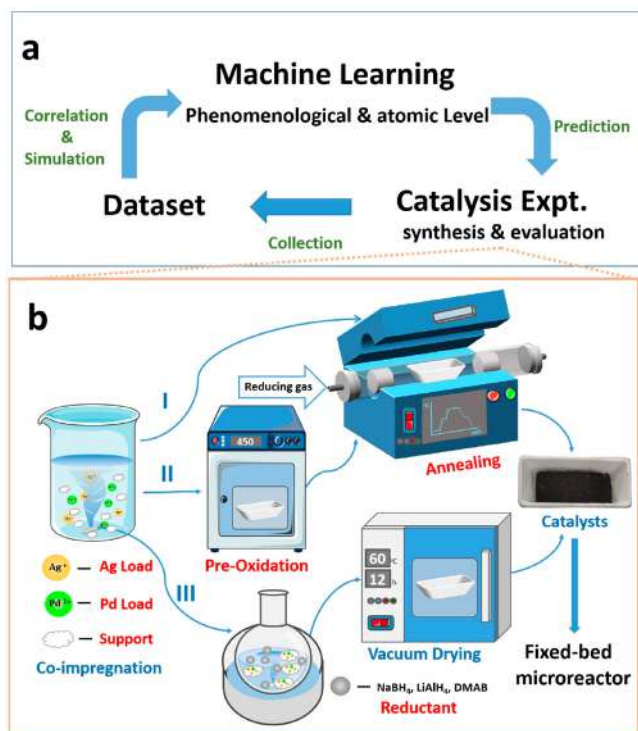


Figure 1. Scheme of a multiscale ML-guided catalyst search where catalyst synthesis procedures via three possible routes are outlined. (a) Relationship between multiscale ML, data set construction and catalysis experiments in our catalyst search. (b) Catalyst synthesis procedures, where the text in red indicates the key variables as the input for the phenomenological-level ML.

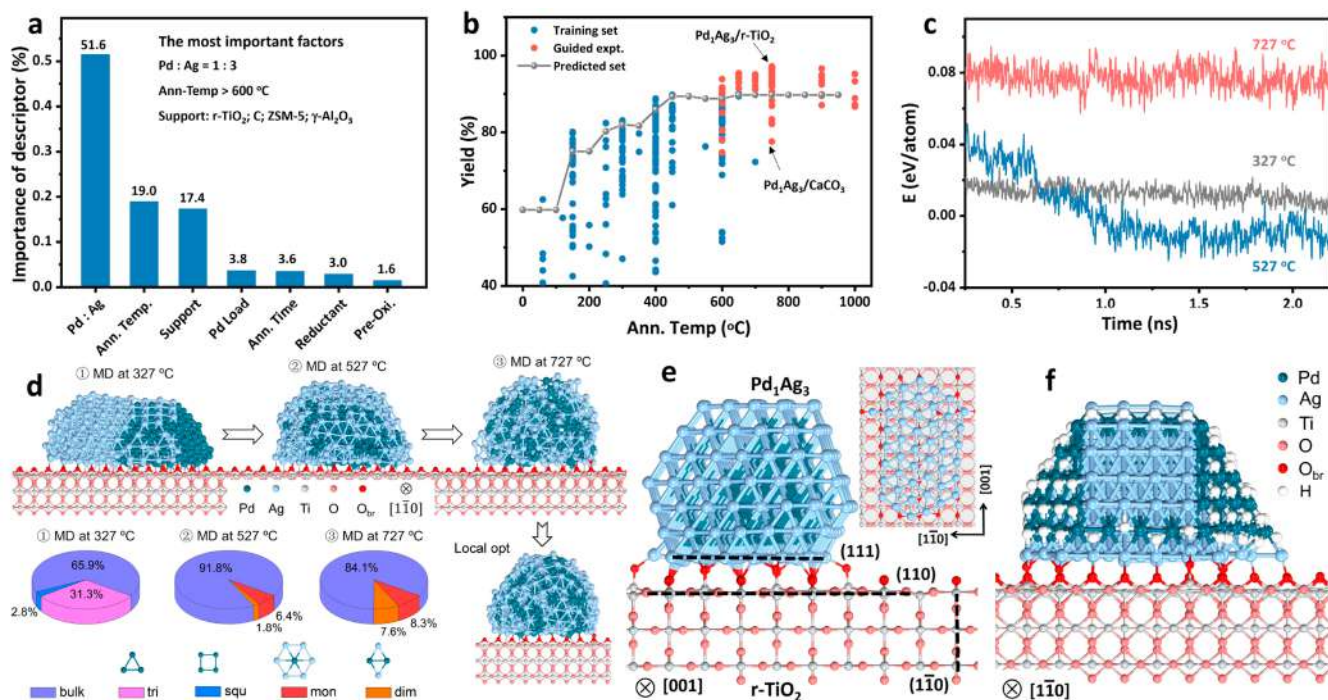


Figure 2. Random forest (RF) ML and large-scale ML atomic simulations for analyzing experimental data and guiding the catalyst search. (a) Feature–importance scores of catalyst descriptors from the RF ML prediction. The more important the feature is, the higher the yield of acetylene semihydrogenation will be. (b) Variations of the yield of acetylene semihydrogenation against the annealing temperature, where the points of the training set (257 samples, blue), the top performance data points at each temperature from a 10000 predicted set (gray), and the ML-guided experiments (106 samples, red) are shown. (c) Potential energy variation of Pd₂₀₈-Ag₂₀₈ supported on r-TiO₂(110) at 327, 527, and 727 °C during the 2.2 ns MD simulations. (d) Final snapshots from the MD final snapshots, where at 727 °C is exemplified. (e, f) Global minimum structures in the absence (e) and presence (f) of H atoms (full coverage) determined by SSW for a Pd₁Ag₃ nanoparticle (Pd₇₀Ag₂₁₀) on r-TiO₂, highlighting the crystalline facets of the alloy. The presence of H will lead to the resurfacing of Pd on the (111) facet, but not on the (100) facet.

ethane selectivity, and yield were calculated by using eqs 1–3, respectively

$$C_{\text{acetylene}} = \frac{C_2\text{H}_2(\text{in}) - C_2\text{H}_2(\text{out})}{C_2\text{H}_2(\text{in})} \times 100\% \quad (1)$$

$$S_{\text{C}_2\text{H}_4} = \left(1 - \frac{C_2\text{H}_6(\text{out}) - C_2\text{H}_6(\text{in})}{C_2\text{H}_2(\text{in}) - C_2\text{H}_2(\text{out})} \right) \times 100\% \quad (2)$$

$$\text{yield} = C_{\text{acetylene}} \times S_{\text{ethylene}} \times 100\% \quad (3)$$

where in/out subscripts refer to the concentrations measured in the inlet/outlet ports. Positive values for C₂H₄ selectivity and yield refer to the net gains of ethylene during the hydrogenation process, whereas negative values represent the C₂H₄ loss.

2.5. Random Forest ML. The *scikit-learn* package (scikit-learn.org) in Python was utilized to build the random forest regression model, which has ten trees with the whole data set to train each tree. The default values were used for common model parameters (e.g., the maximum depth of each tree, the minimum number of samples required to be at a leaf node, etc.). We selected seven different parameters as the input, including the Pd loading (0.01–20%), Ag loading (0.01–30%), the support types assigned to different numbers (1, r-TiO₂; 2, γ-Al₂O₃; 3, ZSM-5; 4, Al-MCM-41; 5, CeO₂; 6, Ti-MOR; 7, α-Al₂O₃; 8, anatase-TiO₂; 9, C; 10, graphene oxide; 11, SAPO-34; 12, Y₂O₃; 13, MCM-41; 14, HT; 15, Ti; 16, Ti-MWW; 17, SiO₂; 18, CaCO₃; 19, P25; 20, ZrO₂; 21, SnO₂; 22,

SiC), the preoxidation condition represented by 1 and 2 (whether calcined in air at 450 °C for 4 h; 1 no and 2 yes), the reductants represented by different numbers (0, no reductant; 1, gaseous 5% H₂; 2, 100% N₂; 3, under vacuum; 4, NaBH₄; 5, dimethylamine; 6, calcination in air; 7, LiAlH₄; 8, 100% CO; 9, 100% H₂), the annealing temperature (150–650 °C), and the annealing time (1–10 h) and the yield of ethylene as the output.

2.6. ML Atomic Simulations. All atomic simulations for Pd–Ag nanoparticles on TiO₂(110) were carried out using the G-NN^{42,43} potential obtained via SSW global PES exploration⁴⁴ as implemented in the large-scale atomic simulation with neural network potential (LASP) package⁴⁰ (www.lasphub.com). The Pd–Ag–Ti–O–H five-element G-NN potential was established by iterative self-learning from the global PES data set, as inherited from the previous first-principles DFT data set of Pd–Ag–H³⁶ and complemented with the new data set for the Pd–Ag–H/TiO₂ composite. The final data set contains 145121 structural configurations covering different Pd–Ag–Ti–O–H compositions that were calculated by DFT (the data set is openly available on the LASP Web site).

To pursue a high accuracy for the PES and speed up the NN training in multielement systems, we adopted a double-net framework as proposed recently,⁴⁵ where Ti, O, and H utilize two neural networks and Pd and Ag utilize a single net. A large set of power-type structure descriptors (PTSD) were utilized to describe the chemical environment for each element. For example, in Pd NN there are 140 two-body, 270 three-body, and 8 four-body PTSDs. Compatibly, a large neural network

with two to three hidden layers (e.g., 418–50–50–1 for Pd/Ag and the first net of Ti/O/H and 229–80–50–50–1 for the second net of Ti/O/H) was generated, involving 192908 network parameters in total. Hyperbolic tangent activation functions were utilized for the hidden layers, while a linear transformation was applied to the output layer of all networks. The final accuracy of the G-NN potential has the energy and force in the root-mean-square errors (RMSE) of 6.146 meV/atom and 0.153 eV/Å respectively, with respect to DFT results.

3. RESULTS AND DISCUSSION

In this work, 257 PdAg catalyst samples were first synthesized to explore the variable space in the experiment. As shown schematically in Figure 1b, a number of experimental conditions that might influence the catalyst performance were modulated in a wide range, including the Pd loading (0.01–20%), Ag loading (0.01–30%), the support (r-TiO₂, C, ZSM-5, γ -Al₂O₃, a-TiO₂, CeO₂, GO, ZrO₂, P2S, SiO₂, CaCO₃, Al-MCM-41, Ti-MOR, SAPO-34, Y₂O₃, HT, MCM-41, and Ti-MWW), the preoxidation condition (whether calcined in air at 450 °C for 4 h prior to reduction), the reductants (including gaseous 5% H₂, 100% H₂, CO, N₂, and air with calcination and NaBH₄, LiAlH₄, and dimethylamine–borane in aqueous solution), the annealing temperature (150–650 °C with an interval of 50 °C), and the annealing time (from 1 to 10 h). All details for the experiments, including the synthetic method and conditions, can be found in Table S1. The catalyst evaluations were carried out in a continuous-flow fixed-bed microreactor in a feed gas consisting of 0.5% C₂H₂, 50.0% C₂H₄, 5.0% H₂, 4.0% He, and 40.5% N₂ at a space velocity of 96,000 mL g⁻¹ h⁻¹, the typical industrial condition. The performances of the catalysts were evaluated using the ethylene yield (the activity multiplies by the selectivity; see eqs 1–3) at the highest acetylene conversion by controlling the reaction temperature.

With these experimental data, a phenomenological-level ML using the random forest (RF) model was utilized to find the correlation between synthesis conditions and catalyst performance. A series of descriptors were designed to distinguish different catalysts, including the chemical compositions of the catalysts (Pd:Ag ratio, supporter type, and Pd loading) and those related to the synthetic conditions (annealing temperature, annealing time, preoxidation, and reductant), which were confirmed to be linearly independent by a Pearson correlation analysis (with the absolute value of correlation coefficients <0.4, see Figure S1). The RF model was trained using these catalyst descriptors as input and the selectivity of acetylene hydrogenation as output, based on 90% of the experimental data: i.e., 231 samples. As shown in Figure S2, the data fit well by the RF model with the R² being 0.91 and 0.87 on the training data and the test data (the remaining 10% of the samples), respectively.

Figure 2a shows the importance ranking for the catalyst descriptors discovered by the RF model, where the Pd:Ag ratio is, not surprisingly, the most important descriptor for ethylene yield, followed by the annealing temperature and the supporter type. While the significance of Pd:Ag ratio (weight 51.6%) was rationalized by our previous work,³⁶ the great influence of the annealing temperature was unexpected, which together with the support material and the weight of 36.4% in total for the catalyst performance, thus points to new directions for catalyst design.

To quantify the catalyst design, we generated randomly 10000 hypothetical experimental conditions and utilized the

RF model to predict their catalyst performance, as shown in Figure 2b, where the variation of ethylene yield is plotted against the annealing temperature, for both the training data set (blue points) and the predicted hypothetical experiments (gray points for only the highest yield at each annealing temperature). It predicts that when the annealing temperature is below 600 °C, the higher the annealing temperature, the higher the selectivity, and the selectivity reaches a plateau of 89.7% above 600 °C, which corresponds to a Pd₁Ag₃ catalyst supported on r-TiO₂ with 1% Pd loading, annealed at 650 °C for 4 h. This prediction steered us to focus on the high annealing temperature and the type of support, which should determine collectively the catalyst morphology and surface structure. The ML atomic simulations of the PdAg/TiO₂ composite and ML-guided catalysis experiments were thus performed to reveal the metal–support interaction and validate theoretical predictions.

The large-scale atomic simulations of complex materials now become feasible with the advent of global neural network (G-NN) potential as practiced by us in recent years,^{46–48} which is several orders of magnitude (>10⁴) faster than traditional DFT calculations but with comparable accuracy. To simulate the PdAg/TiO₂ composite, we generated a Pd–Ag–Ti–O–H five-element G-NN potential by inheriting the previous first-principles data set for Pd–Ag–H and adding the new data set for Pd–Ag–H³⁶ nanoparticles on the TiO₂ material. The G-NN potential was established by iteratively learning from the global potential energy surface (PES) of different Pd–Ag–H composition clusters on TiO₂ surfaces, as sampled by a stochastic surface walking (SSW) exploration^{44,49} (The SSW-NN method and the generation of G-NN potential are detailed in Supporting Information, and the data set for G-NN training is summarized in Table S2.) Based on the Pd–Ag–Ti–O–H G-NN potential, we performed a series of long-term molecular dynamics (MD) simulations using the isothermal Nose–Hoover method from 27 to 827 °C at an interval of 100 °C (simulation time >2.2 ns at each temperature) to follow the structure evolution from low to high temperatures. All MD simulations were carried out in a *p*(20 × 5) (59.4 Å × 33.0 Å) r-TiO₂(110) supercell, starting from the initial structure with two separated nanoparticles, Pd₂₀₈ (~2 nm) and Ag₂₀₈ (~2 nm) (2216 atoms in total). For comparison, similar simulations from individual Pd and Ag particles were also performed, from which the melting point of the nanoparticle was determined. The main theoretical results are summarized in Figure 2c–e, which are elaborated in the following.

Our MD results show that below 227 °C there is no significant interaction between Pd and Ag nanoparticles (see Figure S3), as they remain separated. At 327 °C, the Ag nanoparticle first undergoes a dramatic morphology change, where the local Ag–Ag bonds break with the Ag atoms starting to flow to the nearby Pd nanoparticles and then climb over the Pd surfaces, as shown in the first snapshot in Figure 2d. At this temperature, the mixing of Ag and Pd is very slow with no sign of forming a face-centered-cubic (fcc) PdAg alloy in the 2.2 ns simulation time; the Pd nanoparticle continues to expose large surface areas with both Pd triangles (31.3%, feature of the {111} facet) and Pd squares (2.8%, feature of the {100} facet), as summarized in the pie plot for Pd sites in Figure 2d. It should be mentioned that 327 °C is already close to the melting point of the Ag₂₀₈ nanoparticle (~377 °C from our MD simulations; see Figure S4), which explains why an Ag nanoparticle can break the Ag–Ag bonds and diffuse onto the

surface of a Pd nanoparticle. We also note that both Pd and Ag atoms tend to bond to the protruding bridge O (O_{br}) of $r\text{-TiO}_2(110)$, instead of the atoms in the groove (see the statistical data from the last 0.2 ns simulations in Table S3). Despite the formed Pd– O_{br} and Ag– O_{br} bonds, the $r\text{-TiO}_2(110)$ surface is largely intact during the simulation at 327 °C.

As the temperature was elevated to 527 °C, the whole Ag nanoparticle disappears with all Ag atoms migrating onto the Pd nanoparticle within ~ 1 ns, accompanied by a continuous drop in potential energy (see Figure 2c). The Pd atoms remain largely immobile during 2.2 ns since the temperature is still far below the melting point of Pd_{208} (~ 777 °C from our MD simulation; see Figure S5). While the surface Ag atoms have difficulty in dissolving into the Pd bulk that requires breaking the Pd–Pd bonds, a few Pd sites (4.4% monomer and 1.9% dimer; see Figure 2d bottom pie plot) remain exposed on the surface. When the temperature arrives at 727 °C, the surface Ag atoms quickly dissolve into the Pd bulk within ~ 0.1 ns, which yields finally a uniform but rather disordered PdAg alloy. Compared to 527 °C, there are more Pd monomer (8.3%) and dimer (7.6%) sites exposed, although the Ag atoms are still rich on the surface due to their smaller surface energy. It is notable that, during the alloy formation, the bottom layer of the PdAg nanoparticle is gradually taken over by Ag atoms to interact with $\text{TiO}_2(110)$ (see Table S3), indicating the higher affinity between Ag and TiO_2 . Importantly, O_{br} atoms now diffuse out from the original (110) bridging row to the five-coordinated Ti site (the terminal O) at 727 °C, which helps to stabilize the PdAg nanoparticle by forming stronger metal–O bonds (Figure S6).

To obtain the crystalline alloy structure quenched after annealing, we then utilized an SSW global optimization to search for the global minimum (GM) for differently sized Pd_1Ag_3 nanoparticles on $r\text{-TiO}_2(110)$. We found that the GMs of small alloy nanoparticles (<1 nm) in general do not have an fcc packing form, whereas large alloy nanoparticles adopt the Pd_1Ag_3 fcc crystal. As a representative, the determined GM for a $\text{Pd}_{70}\text{Ag}_{210}$ nanoparticle (~ 2 nm) is shown in Figure 2e. All surfaces and the interface (the bottom layer) of the nanoparticle are covered by Ag atoms, and importantly, the interface Ag layer adopts the (111) facet, where the reconstructed terminal O at the five-coordinated Ti site helps to stabilize the particle edge via Ag–O bonds. This yields an orientation relation between a Pd_1Ag_3 nanoparticle and $r\text{-TiO}_2$ as $\text{PdAg}(111)//\text{TiO}_2(110)$, where $\text{PdAg}[1\bar{1}0]$ is roughly in parallel with $\text{TiO}_2[001]$, suggesting the epitaxial growth of $\text{Pd}_1\text{Ag}_3(111)$ on $r\text{-TiO}_2(110)$ (see Figure 2e, inset). It should be mentioned that we also performed an SSW structure search for Pd_1Ag_3 nanoparticles supported on $a\text{-TiO}_2(101)$, the most stable surface of anatase, and did not find the special crystallographic correspondence.

In contrast, under the hydrogenation conditions where H_2 is rich, Pd atoms become energetically favorable to locate on the surface due to the formation of surface Pd–H bonds. This occurs only on (111) facets at Pd:Ag = 1:3 (see Figure 2f), which then creates mainly two types of surface Pd patterns (i.e., 90.9% Pd triangles on (111) and 9.1% Pd lines at the edges), both being the active sites for acetylene semihydrogenation. As also shown in our previous work,³⁶ the ethane formation via ethylene hydrogenation has a higher barrier (>0.91 eV) at these (111) sites compared to that on the surface Pd sites on (100) surfaces.

On the experiment side, with the guidance of RF prediction (gray line Figure 2b) and the determination of the PdAg alloying temperature (>727 °C) from atomic simulation, we have further synthesized a series of Pd_1Ag_3 catalysts (106 samples, see Table S4 and Figure S7 for details on the experiments) on different supports annealed at relatively high temperatures (600–1000 °C), as also plotted in Figure 2b (the red points), and evaluated their catalytic performance.

Taking $r\text{-TiO}_2$, the best support discovered, as an example, Figure 3a highlights the variation of the selectivity with respect

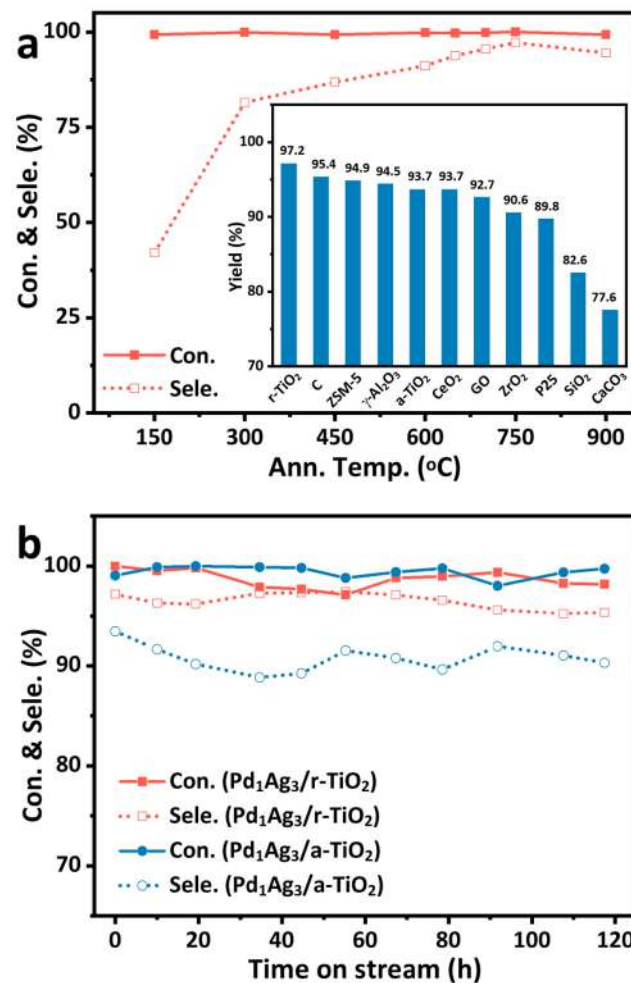


Figure 3. Catalytic performance for acetylene semihydrogenation on $\text{Pd}_1\text{Ag}_3/r\text{-TiO}_2$ catalysts. (a) Selectivity and reaction temperature of the $\text{Pd}_1\text{Ag}_3/r\text{-TiO}_2$ catalysts synthesized at different annealing temperatures. The 750 °C annealed sample achieves a 97.2% selectivity with 100% conversion at 98 °C. The inset compares the yield to ethylene of Pd_1Ag_3 on 11 different supports after annealing at 750 °C. (b) Long-term activity and selectivity of $\text{Pd}_1\text{Ag}_3/r\text{-TiO}_2$ and $\text{Pd}_1\text{Ag}_3/a\text{-TiO}_2$ catalysts for acetylene semihydrogenation.

to the annealing temperatures. $\text{Pd}_1\text{Ag}_3/r\text{-TiO}_2$ exhibits a sharp increase of selectivity from 42.1% to 97.2% with an increase in annealing temperature from 150 to 750 °C, and a further increase in temperature to 900 °C slightly reduces the selectivity to 85.5%. The best sample thus corresponds to that annealed at 750 °C (T_{750} sample), which achieves 97.2% selectivity at 98 °C with 100% conversion. The high annealing temperature required for the PdAg catalyst is consistent with the start-up temperature (727 °C) of PdAg bulk alloy

formation from our atomic simulations. It should be mentioned that the annealing temperatures with an H_2 atmosphere reported in the literature are generally around 150–600 °C,^{9,10,50} which are not sufficient to create PdAg bulk alloys. As shown in the inset of Figure 3a, the r-TiO₂ support has a yield of acetylene hydrogenation 20% higher than that of the CaCO₃ support (77.6%). For catalysts on different support materials with the same Pd₁Ag₃ composition and the high annealing temperature (≥ 750 °C), the top 30 samples in Figure 2b, their performances are generally good ($\geq 93.0\%$ selectivity), ranking in the top 10% among all 363 samples, and higher than those of most of the reported catalysts in the literature (see Table S5).^{2,27,36,51–59}

Next, the long-term stability and performance of the Pd₁Ag₃/r-TiO₂ and Pd₁Ag₃/a-TiO₂ catalysts were evaluated over a 120 h hydrogenation experiment by maintaining the high conversion, as shown in Figure 3b. We found that the selectivity is rather stable, above 95% (Pd₁Ag₃/r-TiO₂) at the high conversion ($>98\%$), which is consistently higher than that of Pd₁Ag₃ on a-TiO₂ (88%), suggesting the special promoting role of the crystal surface registry between r-TiO₂ and Pd₁Ag₃ nanoparticles, PdAg(111)//TiO₂(110). The ethylene oligomerization products and the “green oil” droplets (mainly long-chain hydrocarbons) are not found in the outlet products, reflecting that the catalyst is not poisoned over the long-term high-conversion test. Our TEM investigation also confirmed that the surface morphology of metal nanoparticles maintains a clear-cut surface edge after the long-term experiment (Figure S8). The likely surface structure evolution (Pd–Ag exchange and surface reconstruction) due to the adsorption of acetylene and H species^{34,36} thus does not markedly affect the activity and selectivity.

To provide a deeper understanding of the catalyst structure evolution in synthesis and compare them with the atomic simulation results, we prepared a series of Pd₁Ag₃/r-TiO₂ catalysts by the coimpregnation of Pd(NO₃)₂ and AgNO₃ (Pd:Ag = 1:3) on r-TiO₂ followed by annealing under a 5% H₂ atmosphere at different temperatures from 150 to 900 °C (T150 to T900 samples). Figure 4a shows the X-ray diffraction (XRD) patterns for the samples: at low temperatures (e.g., 150 °C), only two peaks of r-TiO₂ are visible at 36.07 and 41.14°, being the {101} and {111} planes of r-TiO₂, respectively. At 750 °C two new peaks appear at 38.63 and 44.82°, which are assigned to the {111} and {200} planes of Pd₁Ag₃, respectively, based on theoretical values (38.65 and 44.90°) of the Pd₁Ag₃ crystal (*Pm* $\bar{3}$ *m*, *a* = 4.09 Å),³⁶ which indicates the formation of a Pd₁Ag₃ crystal. Our further *in situ* XRD shows that these new peaks of PdAg alloy emerge above 650 °C on r-TiO₂ (see Figure S9). It might be mentioned that the Pd₁Ag₃ crystal forms above 750 °C irrespective of the support material, as shown in Figure S10a–q from the XRD patterns of catalysts with different supports.

Figure 4b shows the temperature-programmed desorption (TPD) of CO on Pd₁Ag₃/r-TiO₂ samples from 30 to 500 °C, which provides further information on the exposed Pd sites of the catalyst (CO adsorption on Ag is too weak to detect in TPD). For the low-temperature sample, e.g., T150, CO desorption peaks are broadly divided into two peaks at 250 and 360 °C, which correspond to CO adsorption at the top site and the hollow site, respectively.^{60,61} With an increase in annealing temperature, the surface Pd gradually disappears and thus the CO desorption peak intensity drops significantly, suggesting the agglomeration of Pd particles and then Ag

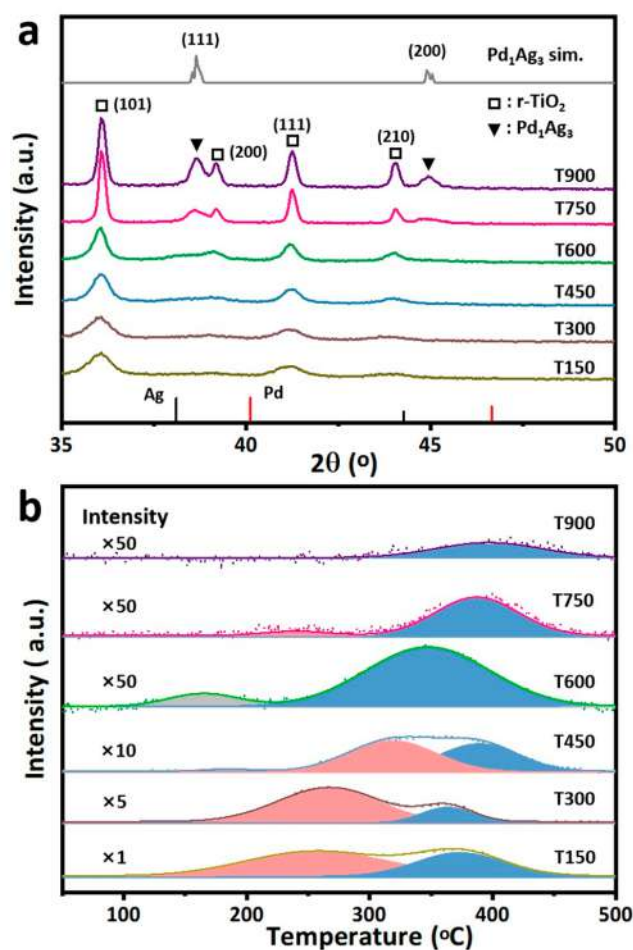


Figure 4. Characterization of Pd₁Ag₃/r-TiO₂ catalysts synthesized at annealing temperatures from 150 to 900 °C. (a) XRD pattern together with the theoretically simulated pattern of a Pd₁Ag₃ crystal. (b) CO-TPD profiles, where the intensity is amplified by 5–50 times at elevated temperatures for clarity.

covering of Pd particles. For the high-temperature samples, e.g., T750, only a small peak at ~ 390 °C is left, which corresponds to CO at the hollow site of Pd, which can be readily assigned to the CO adsorption at minority Pd-triangle sites surrounded by Ag atoms that form via the Pd–Ag surface exchange.

The TEM image of the T750 sample, shown in Figure 5a, indicates that the metal nanoparticles are finely distributed. The elemental mapping in Figure 5b demonstrates that Pd and Ag are uniformly distributed in the nanoparticles. Energy dispersive X-ray spectroscopy (EDX) determines the ratio of Pd:Ag to be 25.2:74.8 (see the inset), close to the stoichiometry 1:3. In fact, the actual metal loading for Pd₁Ag₃/r-TiO₂ catalysts after different reduction temperatures (T150, T450, T600, T750, T900) was also confirmed by inductive coupled plasma (ICP) optical emission and their Pd:Ag atomic ratios are all close to 1:3, which agrees well with the designed ratio (see Table S6). Besides, the spatial elemental distribution of the Pd₁Ag₃ nanoparticle was measured by high-angle annular dark-field scanning TEM (HAADF-STEM) combined with EDX (Figure 5c). Along the scanning line, the EDX spectrum of Ag is slightly wider than that of Pd, which indicates that Ag is enriched on the surface of the nanoparticle, especially on the side attaching to the r-TiO₂

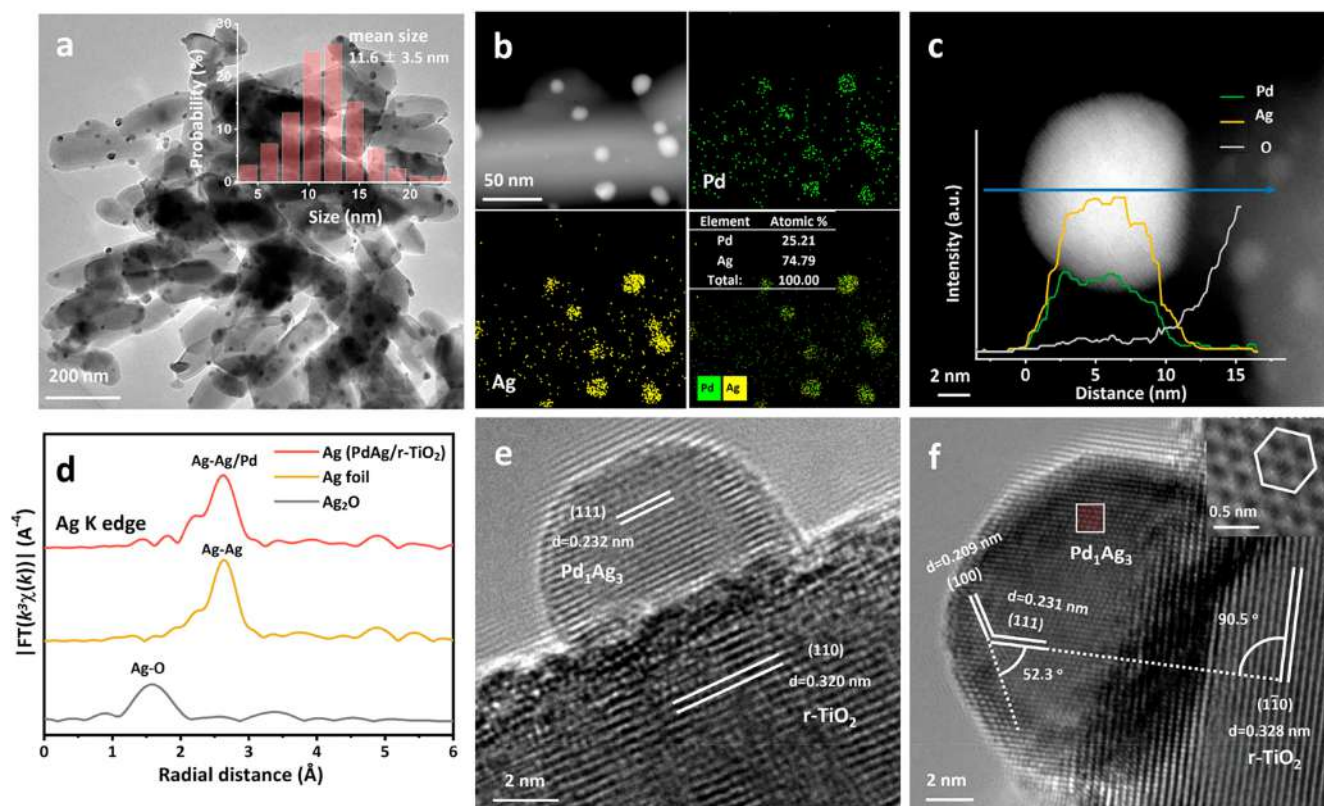


Figure 5. Structure and composition characterizations of the Pd₁Ag₃/r-TiO₂ (T750) catalyst. (a) TEM images and particle size distributions. (b) STEM and STEM-EDX element mapping. (c) HAADF-STEM image and corresponding EDX line scan. (d) Ag K-edge EXAFS spectra in real space. (e, f) HRTEM images of two typical PdAg nanoparticles in contact with r-TiO₂. The inset is the magnified image of the rectangular region in (f).

(i.e., the right side in the image). This picture confirms the dominance of Ag on the PdAg alloy surface and the enrichment of Ag at the r-TiO₂ interface. The real-space extended X-ray absorption fine structure (EXAFS) in Figure 5d together with Figures S11–S14 and Table S7 also confirm the alloy Pd₁Ag₃ crystal formation of the T750 sample: each Ag atom has 8 Ag first neighbors (Ag–Ag distance 2.89 Å) and 3.9 Pd first neighbors (Ag–Pd distance 2.85 Å), whereas Pd atoms are separated by Ag first neighbors (Pd–Ag distance 2.72 Å). EXAFS (Figure S13) also detects the presence of Pd–O species, suggesting the oxidation of surface Pd in catalysts during sample transfer and the necessity of the prerduction in catalysis.

Two typical Pd–Ag nanoparticles in contact with r-TiO₂ have been carefully analyzed using high-resolution transmission electron microscopy (HRTEM), as shown in Figure 5e,f. They are relatively large in size, and thus an atomic resolution for the PdAg alloy (~0.231 nm spacing for the close-packed {111} planes) and r-TiO₂ (0.328 nm spacing for {110} planes) can be clearly achieved. Both nanoparticles follow the same orientation relation where a PdAg nanoparticle of a {111} plane parallel to r-TiO₂{110} (Figure 5e) and perpendicular to the {110} plane of r-TiO₂ (Figure 5f). This agrees perfectly with the theoretical results in Figure 2e.

The collective evidence from theory and experiment here complements our previous work³⁶ that focused on the activity and selectivity of different crystal facets of PdAg alloy, and now a full rationalization can finally be achieved to understand the high performance of the high-temperature-annealed Pd₁Ag₃/r-TiO₂ catalyst. A Pd₁Ag₃ alloy crystal forms above 727 °C,

where all surfaces and the metal/TiO₂ interface are terminated by Ag atoms. Because the interface Ag layer adopts the {111} close-packed plane, the PdAg nanoparticles prefer to epitaxially grow on r-TiO₂{110} to maximally expose the desired {111} facets, where Pd atoms will resurface in the hydrogenation reaction, as shown in Figure 2f and also our previous thermodynamic diagram.³⁶ Our microkinetics simulations based on the DFT kinetics data reported previously indicate that the high {111}:{100} ratio of the nanoparticle is the key to achieving high selectivity: as the {111}:{100} ratio increases from 60:1 to 160:1, the acetylene selectivity can increase from 82.56% to 97.19% (see Figure S15). The high annealing temperature and the r-TiO₂ support are thus critical for melting Pd nanoparticles to form Pd₁Ag₃ alloy crystals, creating an epitaxial growth mode of the alloy/oxide interface and thus controlling the {111}:{100} ratio of alloy nanoparticles for the catalytic selectivity.

It is worth comparing our catalyst with other state-of-the-art Pd-based catalysts that have high activity and selectivity. In particular, Zou et al.²⁷ recently reported a Pd_{1.0}/Bi₂O₃/TiO₂ catalyst synthesized by a two-step photodeposition method, which can achieve 91% selectivity to ethylene and 90% conversion of acetylene below 50 °C. Under these reaction conditions, 1 g of palladium can completely convert 45.8 mol of acetylene to ethylene in 1 day, close to the amount in our work (50.0 mol g_{Pd}⁻¹). Besides, Liu et al.⁵⁹ reported that with Ga₂O₃ coating using the ALD method, an Ag@Pd core-shell bimetallic nanoparticle catalyst can achieve 95% selectivity, but at a higher temperature of ~120 °C. Their mass-specific activity is apparently the highest, being 61.1 mol g_{Pd}⁻¹.

Compared to these state-of-the-art catalysts, our catalyst has a simpler topological structure and can work at a low (0.5%) acetylene ratio in ethylene, showing the great potential for large-scale applications in industry.

4. CONCLUSIONS

By combining experiment and multiscale ML techniques, this work reaches a new record for low-temperature acetylene semihydrogenation: namely, 97.2% selectivity below 100 °C at 100% conversion for 1% acetylene in ethene. Compared to our previous work³⁶ with ~85% selectivity, the appreciable increase in selectivity is attributed first to the high annealing temperature (>750 °C) that leads to the formation of a Pd₁Ag₃ alloy crystal, as revealed from RF predictions based on the experimental database and ML atomic simulations for nanoparticle structure evolution on the oxide surface. In addition to Pd₁Ag₃ alloy crystal formation, the presence of a special crystallographic correspondence between a Pd₁Ag₃ alloy nanoparticle and r-TiO₂ is identified from both theory and experiment as another important factor to boost the selectivity, namely, with a PdAg(111)//TiO₂(110) orientation relationship, suggesting the preferentially exposed (111) via the epitaxial growth mode. Our work not only leads to the finding of a high-performance acetylene semihydrogenation catalyst but also demonstrates the great promise for the rational design of complex heterogeneous catalytic systems by exploiting multiscale machine-learning techniques.

■ ASSOCIATED CONTENT

SI Supporting Information

The Supporting Information is available free of charge at <https://pubs.acs.org/doi/10.1021/acscatal.2c04379>.

Additional experimental details, SSW-NN method and the generation of Pd–Ag–Ti–C–H G-NN potential, random forest ML, ML atomic simulations for Pd–Ag nanoparticles on TiO₂, morphology characterization of Pd₁Ag₃ alloy on different supports, TEM of Pd₁Ag₃/r-TiO₂(T750) after a long-term hydrogenation experiment, XRD spectra of Pd₁Ag₃ alloy on different supports, EXAFS results for the Pd₁Ag₃/r-TiO₂(T750) catalyst, microkinetic simulations, experimental data set for RF ML, structural information on the global PES data set for G-NN potential training, statistics for MD simulations of PdAg nanoparticles on TiO₂ at different temperatures, experimental results guided by multiscale ML, and acetylene hydrogenation catalysts in the literature and their performance (PDF)

■ AUTHOR INFORMATION

Corresponding Author

Zhi-Pan Liu – Collaborative Innovation Center of Chemistry for Energy Materials (iChEM), Shanghai Key Laboratory of Molecular Catalysis and Innovative Materials, Key Laboratory of Computational Physical Science, Department of Chemistry, Fudan University, Shanghai 200433, People's Republic of China; Key Laboratory of Synthetic and Self-Assembly Chemistry for Organic Functional Molecules, Shanghai Institute of Organic Chemistry, Chinese Academy of Sciences, Shanghai 200032, People's Republic of China; orcid.org/0000-0002-2906-5217; Email: zpliu@fudan.edu.cn

Authors

Lin Chen – Collaborative Innovation Center of Chemistry for Energy Materials (iChEM), Shanghai Key Laboratory of Molecular Catalysis and Innovative Materials, Key Laboratory of Computational Physical Science, Department of Chemistry, Fudan University, Shanghai 200433, People's Republic of China

Xiao-Tian Li – Collaborative Innovation Center of Chemistry for Energy Materials (iChEM), Shanghai Key Laboratory of Molecular Catalysis and Innovative Materials, Key Laboratory of Computational Physical Science, Department of Chemistry, Fudan University, Shanghai 200433, People's Republic of China

Sicong Ma – Key Laboratory of Synthetic and Self-Assembly Chemistry for Organic Functional Molecules, Shanghai Institute of Organic Chemistry, Chinese Academy of Sciences, Shanghai 200032, People's Republic of China; orcid.org/0000-0001-5894-5910

Yi-Fan Hu – Collaborative Innovation Center of Chemistry for Energy Materials (iChEM), Shanghai Key Laboratory of Molecular Catalysis and Innovative Materials, Key Laboratory of Computational Physical Science, Department of Chemistry, Fudan University, Shanghai 200433, People's Republic of China

Cheng Shang – Collaborative Innovation Center of Chemistry for Energy Materials (iChEM), Shanghai Key Laboratory of Molecular Catalysis and Innovative Materials, Key Laboratory of Computational Physical Science, Department of Chemistry, Fudan University, Shanghai 200433, People's Republic of China; orcid.org/0000-0001-7486-1514

Complete contact information is available at: <https://pubs.acs.org/doi/10.1021/acscatal.2c04379>

Author Contributions

L.C. and X.-T.L. contributed equally to this work.

Notes

The authors declare no competing financial interest.

■ ACKNOWLEDGMENTS

This work received financial support from the National Key Research and Development Program of China (2018YFA0208600), the National Science Foundation of China (12188101, 22033003, 91945301, 91745201, 92145302, 22122301, and 92061112), the Fundamental Research Funds for the Central Universities (20720220011), and the Tencent Foundation for XPLOER PRIZE.

■ REFERENCES

- (1) Teschner, D.; Borsodi, J.; Woosch, A.; Revay, Z.; Havecker, M.; Knop-Gericke, A.; Jackson, S. D.; Schlogl, R. The roles of subsurface carbon and hydrogen in palladium-catalyzed alkyne hydrogenation. *Science* **2008**, *320*, 86.
- (2) Studt, F.; Abild-Pedersen, F.; Bligaard, T.; Sorensen, R. Z.; Christensen, C. H.; Norskov, J. K. Identification of non-precious metal alloy catalysts for selective hydrogenation of acetylene. *Science* **2008**, *320*, 1320.
- (3) Kyriakou, G.; Boucher, M. B.; Jewell, A. D.; Lewis, E. A.; Lawton, T. J.; Baber, A. E.; Tierney, H. L.; Flytzani-Stephanopoulos, M.; Sykes, E. C. H. Isolated Metal Atom Geometries as a Strategy for Selective Heterogeneous Hydrogenations. *Science* **2012**, *335*, 1209.
- (4) Armbruster, M.; Kovnir, K.; Friedrich, M.; Teschner, D.; Wowsnick, G.; Hahne, M.; Gille, P.; Szentmiklosi, L.; Feuerbacher, M.; Heggen, M.; Girsig, F.; Rosenthal, D.; Schlogl, R.; Grin, Y.

Al₁₃Fe₄ as a low-cost alternative for palladium in heterogeneous hydrogenation. *Nat. Mater.* **2012**, *11*, 690.

(5) Wei, S. J.; Li, A.; Liu, J. C.; Li, Z.; Chen, W. X.; Gong, Y.; Zhang, Q. H.; Cheong, W. C.; Wang, Y.; Zheng, L. R.; Xiao, H.; Chen, C.; Wang, D. S.; Peng, Q.; Gu, L.; Han, X. D.; Li, J.; Li, Y. D. Direct observation of noble metal nanoparticles transforming to thermally stable single atoms. *Nat. Nanotechnol.* **2018**, *13*, 856.

(6) Zhang, L. L.; Zhou, M. X.; Wang, A. Q.; Zhang, T. Selective Hydrogenation over Supported Metal Catalysts: From Nanoparticles to Single Atoms. *Chem. Rev.* **2020**, *120*, 683.

(7) Bu, J.; Liu, Z. P.; Ma, W. X.; Zhang, L.; Wang, T.; Zhang, H. P.; Zhang, Q. Y.; Feng, X. L.; Zhang, J. Selective electrocatalytic semihydrogenation of acetylene impurities for the production of polymer-grade ethylene. *Nat. Catal.* **2021**, *4*, 557.

(8) Liu, Y. X.; Liu, X. W.; Feng, Q. C.; He, D. S.; Zhang, L. B.; Lian, C.; Shen, R. A.; Zhao, G. F.; Ji, Y. J.; Wang, D. S.; Zhou, G.; Li, Y. D. Intermetallic Ni_xMy (M = Ga and Sn) Nanocrystals: A Non-precious Metal Catalyst for Semi-Hydrogenation of Alkynes. *Adv. Mater.* **2016**, *28*, 4747.

(9) Zhang, Q. W.; Li, J.; Liu, X. X.; Zhu, Q. M. Synergetic effect of Pd and Ag dispersed on Al₂O₃ in the selective hydrogenation of acetylene. *Appl. Catal. a-Gen* **2000**, *197*, 221.

(10) Zea, H.; Lester, K.; Datye, A. K.; Rightor, E.; Gulotty, R.; Waterman, W.; Smith, M. The influence of Pd-Ag catalyst for ethylene hydrogenation restructuring on the activation energy in ethylene-acetylene mixtures. *Appl. Catal. a-Gen* **2005**, *282*, 237.

(11) Khan, N. A.; Shaikhutdinov, S.; Freund, H. J. Acetylene and ethylene hydrogenation on alumina supported Pd-Ag model catalysts. *Catal. Lett.* **2006**, *108*, 159.

(12) Lee, J. H.; Kim, S. K.; Ahn, I. Y.; Kim, W. J.; Moon, S. H. Performance of Pd-Ag/Al₂O₃ catalysts prepared by the selective deposition of Ag onto Pd in acetylene hydrogenation. *Catal. Commun.* **2011**, *12*, 1251.

(13) Han, Y. X.; Peng, D.; Xu, Z. Y.; Wan, H. Q.; Zheng, S. R.; Zhu, D. Q. TiO₂ supported Pd@Ag as highly selective catalysts for hydrogenation of acetylene in excess ethylene. *Chem. Commun.* **2013**, *49*, 8350.

(14) Ball, M. R.; Rivera-Dones, K. R.; Gilcher, E. B.; Ausman, S. F.; Hullfish, C. W.; Lebron, E. A.; Dumesic, J. A. AgPd and CuPd Catalysts for Selective Hydrogenation of Acetylene. *ACS Catal.* **2020**, *10*, 8567.

(15) Shi, R.; Wang, Z. P.; Zhao, Y. X.; Waterhouse, G. I. N.; Li, Z. H.; Zhang, B. K.; Sun, Z. M.; Xia, C. A.; Wang, H. T.; Zhang, T. R. Room-temperature electrochemical acetylene reduction to ethylene with high conversion and selectivity. *Nat. Catal.* **2021**, *4*, 565.

(16) Borodzinski, A.; Bond, G. C. Selective hydrogenation of ethyne in ethene-rich streams on palladium catalysts. Part 1. Effect of changes to the catalyst during reaction. *Catal. Rev.- Sci. Eng.* **2006**, *48*, 91.

(17) Borodzinski, A.; Bond, G. C. Selective hydrogenation of ethyne in ethene-rich streams on palladium catalysts, Part 2: Steady-state kinetics and effects of palladium particle size, carbon monoxide, and promoters. *Catal. Rev.- Sci. Eng.* **2008**, *50*, 379.

(18) McCue, A. J.; Anderson, J. A. Recent advances in selective acetylene hydrogenation using palladium containing catalysts. *Front. Chem. Sci. Eng.* **2015**, *9*, 142.

(19) Li, X. T.; Chen, L.; Shang, C.; Liu, Z. P. Selectivity control in alkyne semihydrogenation: Recent experimental and theoretical progress. *Chinese Journal of Catalysis* **2022**, *43*, 1991.

(20) Armbruster, M.; Wowsnick, G.; Friedrich, M.; Heggen, M.; Cardoso-Gil, R. Synthesis and Catalytic Properties of Nanoparticulate Intermetallic Ga-Pd Compounds. *J. Am. Chem. Soc.* **2011**, *133*, 9112.

(21) Armbruster, M.; Kovnir, K.; Behrens, M.; Teschner, D.; Grin, Y.; Schlogl, R. Pd-Ga Intermetallic Compounds as Highly Selective Semihydrogenation Catalysts. *J. Am. Chem. Soc.* **2010**, *132*, 14745.

(22) Shao, L. D.; Zhang, W.; Armbruster, M.; Teschner, D.; Girgsdies, F.; Zhang, B. S.; Timpe, O.; Friedrich, M.; Schlogl, R.; Su, D. S. Nanosizing Intermetallic Compounds Onto Carbon Nanotubes: Active and Selective Hydrogenation Catalysts. *Angew. Chem., Int. Ed.* **2011**, *50*, 10231.

(23) Feng, Q. C.; Zhao, S.; Wang, Y.; Dong, J. C.; Chen, W. X.; He, D. S.; Wang, D. S.; Yang, J.; Zhu, Y. M.; Zhu, H. L.; Gu, L.; Li, Z.; Liu, Y. X.; Yu, R.; Li, J.; Li, Y. D. Isolated Single-Atom Pd Sites in Intermetallic Nanostructures: High Catalytic Selectivity for Semihydrogenation of Alkynes. *J. Am. Chem. Soc.* **2017**, *139*, 7294.

(24) Cao, Y. Q.; Sui, Z. J.; Zhu, Y.; Zhou, X. G.; Chen, D. Selective Hydrogenation of Acetylene over Pd-In/Al₂O₃ Catalyst: Promotional Effect of Indium and Composition-Dependent Performance. *ACS Catal.* **2017**, *7*, 7835.

(25) Zhou, H. R.; Yang, X. F.; Li, L.; Liu, X. Y.; Huang, Y. Q.; Pan, X. L.; Wang, A. Q.; Li, J.; Zhang, T. PdZn Intermetallic Nanostructure with Pd-Zn-Pd Ensembles for Highly Active and Chemoselective Semi-Hydrogenation of Acetylene. *ACS Catal.* **2016**, *6*, 1054.

(26) Hu, M. Z.; Zhao, S.; Liu, S. J.; Chen, C.; Chen, W. X.; Zhu, W.; Liang, C.; Cheong, W. C.; Wang, Y.; Yu, Y.; Peng, Q.; Zhou, K. B.; Li, J.; Li, Y. D. MOF-Confined Sub-2 nm Atomically Ordered Intermetallic PdZn Nanoparticles as High-Performance Catalysts for Selective Hydrogenation of Acetylene. *Adv. Mater.* **2018**, *30*, 1801878.

(27) Zou, S. H.; Lou, B. H.; Yang, K. R.; Yuan, W. T.; Zhu, C. Z.; Zhu, Y. H.; Du, Y. H.; Lu, L. F.; Liu, J. J.; Huang, W. X.; Yang, B.; Gong, Z. M.; Cui, Y.; Wang, Y.; Ma, L.; Ma, J. Y.; Jiang, Z.; Xiao, L. P.; Fan, J. Grafting nanometer metal/oxide interface towards enhanced low-temperature acetylene semi-hydrogenation. *Nat. Commun.* **2021**, *12*, 1.

(28) Lou, B. H.; Kang, H. Q.; Yuan, W. T.; Ma, L.; Huang, W. X.; Wang, Y.; Jiang, Z.; Du, Y. H.; Zou, S. H.; Fan, J. Highly Selective Acetylene Semihydrogenation Catalyst with an Operation Window Exceeding 150 degrees C. *ACS Catal.* **2021**, *11*, 6073.

(29) Bridier, B.; Perez-Ramirez, J. Cooperative Effects in Ternary Cu-Ni-Fe Catalysts Lead to Enhanced Alkene Selectivity in Alkyne Hydrogenation. *J. Am. Chem. Soc.* **2010**, *132*, 4321.

(30) Kojima, T.; Kameoka, S.; Fujii, S.; Ueda, S.; Tsai, A. P. Catalysis-tunable Heusler alloys in selective hydrogenation of alkynes: A new potential for old materials. *Sci. Adv.* **2018**, *4*, eaat6063.

(31) Niu, Y. M.; Huang, X.; Wang, Y. Z.; Xu, M.; Chen, J. A.; Xu, S. L.; Willinger, M. G.; Zhang, W.; Wei, M.; Zhang, B. S. Manipulating interstitial carbon atoms in the nickel octahedral site for highly efficient hydrogenation of alkyne. *Nat. Commun.* **2020**, *11*, 1.

(32) Doyle, A. M.; Shaikhutdinov, S. K.; Jackson, S. D.; Freund, H. J. Hydrogenation on metal surfaces: Why are nanoparticles more active than single crystals? *Angew. Chem., Int. Ed.* **2003**, *42*, 5240.

(33) Wilde, M.; Fukutani, K.; Ludwig, W.; Brandt, B.; Fischer, J. H.; Schauermaier, S.; Freund, H. J. Influence of Carbon Deposition on the Hydrogen Distribution in Pd Nanoparticles and Their Reactivity in Olefin Hydrogenation. *Angew. Chem., Int. Ed.* **2008**, *47*, 9289.

(34) Li, X. T.; Chen, L.; Wei, G. F.; Shang, C.; Liu, Z. P. Sharp Increase in Catalytic Selectivity in Acetylene Semihydrogenation on Pd Achieved by a Machine Learning Simulation-Guided Experiment. *ACS Catal.* **2020**, *10*, 9694.

(35) Karakaya, I.; Thompson, W. T. The Ag-Pd (Silver-Palladium) system. *Bull. Alloy Phase Diagrams* **1988**, *9*, 237.

(36) Li, X. T.; Chen, L.; Shang, C.; Liu, Z. P. In Situ Surface Structures of PdAg Catalyst and Their Influence on Acetylene Semihydrogenation Revealed by Machine Learning and Experiment. *J. Am. Chem. Soc.* **2021**, *143*, 6281.

(37) Wouda, P. T.; Schmid, M.; Nieuwenhuys, B. E.; Varga, P. STM study of the (111) and (100) surfaces of PdAg. *Surf. Sci.* **1998**, *417*, 292.

(38) Lim, J. S.; Vandermause, J.; van Spronsen, M. A.; Musaelian, A.; Xie, Y.; Sun, L. X.; O'Connor, C. R.; Egle, T.; Molinari, N.; Florian, J.; Duanmu, K.; Madix, R. J.; Sautet, P.; Friend, C. M.; Kozinsky, B. Evolution of Metastable Structures at Bimetallic Surfaces from Microscopy and Machine-Learning Molecular Dynamics. *J. Am. Chem. Soc.* **2020**, *142*, 15907.

(39) Breiman, L. Random forests. *Machine Learning* **2001**, *45*, 5.

(40) Huang, S. D.; Shang, C.; Kang, P. L.; Zhang, X. J.; Liu, Z. P. LASP: Fast global potential energy surface exploration. *WIREs Comput. Mol. Sci.* **2019**, *9*, e1415.

- (41) Huang, Q.; Gao, L. A simple route for the synthesis of rutile TiO₂ nanorods. *Chem. Lett.* **2003**, *32*, 638.
- (42) Huang, S. D.; Shang, C.; Zhang, X. J.; Liu, Z. P. Material discovery by combining stochastic surface walking global optimization with a neural network. *Chem. Sci.* **2017**, *8*, 6327.
- (43) Huang, S. D.; Shang, C.; Kang, P. L.; Liu, Z. P. Atomic structure of boron resolved using machine learning and global sampling. *Chem. Sci.* **2018**, *9*, 8644.
- (44) Shang, C.; Liu, Z. P. Stochastic Surface Walking Method for Structure Prediction and Pathway Searching. *J. Chem. Theory Comput.* **2013**, *9*, 1838.
- (45) Kang, P. L.; Shang, C.; Liu, Z. P. Recent Implementations in LASP 3.0: Global Neural Network Potential with Multiple Elements and Better Long-Range Description. *Chin. J. Chem. Phys.* **2021**, *34*, 583.
- (46) Liu, Q. Y.; Shang, C.; Liu, Z. P. In Situ Active Site for CO Activation in Fe-Catalyzed Fischer–Tropsch Synthesis from Machine Learning. *J. Am. Chem. Soc.* **2021**, *143*, 11109.
- (47) Ma, S. C.; Liu, Z. P. Zeolite-confined subnanometric PtSn mimicking mortise-and-tenon joinery for catalytic propane dehydrogenation. *Nat. Commun.* **2022**, *13*, 1.
- (48) Shi, Y.-F.; Kang, P.-L.; Shang, C.; Liu, Z.-P. Methanol Synthesis from CO₂/CO Mixture on Cu-Zn Catalysts from Microkinetics-Guided Machine Learning Pathway Search. *J. Am. Chem. Soc.* **2022**, *144*, 13401.
- (49) Shang, C.; Zhang, X. J.; Liu, Z. P. Stochastic surface walking method for crystal structure and phase transition pathway prediction. *Phys. Chem. Chem. Phys.* **2014**, *16*, 17845.
- (50) Jin, Y. M.; Dartye, A. K.; Rightor, E.; Gulotty, R.; Waterman, W.; Smith, M.; Holbrook, M.; Maj, J.; Blackson, J. The influence of catalyst restructuring on the selective hydrogenation of acetylene to ethylene. *J. Catal.* **2001**, *203*, 292.
- (51) Ma, R.; He, Y.; Feng, J.; Hu, Z.-Y.; Van Tendeloo, G.; Li, D. A facile synthesis of Ag@PdAg core-shell architecture for efficient purification of ethene feedstock. *J. Catal.* **2019**, *369*, 440.
- (52) Pei, G. X.; Liu, X. Y.; Wang, A.; Lee, A. F.; Isaacs, M. A.; Li, L.; Pan, X.; Yang, X.; Wang, X.; Tai, Z.; Wilson, K.; Zhang, T. Ag Alloyed Pd Single-Atom Catalysts for Efficient Selective Hydrogenation of Acetylene to Ethylene in Excess Ethylene. *ACS Catal.* **2015**, *5*, 3717.
- (53) Li, Q.; Wang, Y.; Skoptsov, G.; Hu, J. Selective Hydrogenation of Acetylene to Ethylene over Bimetallic Catalysts. *Ind. Eng. Chem. Res.* **2019**, *58*, 20620.
- (54) Liu, Y.; Zhao, J.; He, Y.; Feng, J.; Wu, T.; Li, D. Highly efficient PdAg catalyst using a reducible Mg-Ti mixed oxide for selective hydrogenation of acetylene: Role of acidic and basic sites. *J. Catal.* **2017**, *348*, 135.
- (55) Che, C.; Wang, B.; Shan, C.; Chen, H.; Liu, W.; Tang, Y. An Effective Strategy to Prepare Pd-Ag/MgCO₃@α-Al₂O₃ Catalyst for Selective Hydrogenation of Acetylene. *Catal. Lett.* **2017**, *147*, 483.
- (56) Takht Ravanchi, M.; Rahimi Fard, M.; Sahebdehfar, S.; Bigdeli, P. Synthesis of Pd-Ag/Al₂O₃ catalyst by colloidal oxide method for acetylene selective hydrogenation: a study on the sintering of PdO nanoparticles. *Res. Chem. Intermed.* **2022**, *48*, 817.
- (57) Smirnova, N. S.; Markov, P. V.; Baeva, G. N.; Rassolov, A. V.; Mashkovsky, I. S.; Bukhtiyarov, A. V.; Prosvirin, I. P.; Panafidin, M. A.; Zubavichus, Y. V.; Bukhtiyarov, V. I.; Stakheev, A. Y. CO-induced segregation as an efficient tool to control the surface composition and catalytic performance of PdAg₃/Al₂O₃ catalyst. *Mendeleev Commun.* **2019**, *29*, 547.
- (58) Glyzdova, D. V.; Afonassenko, T. N.; Khramov, E. V.; Leont'eva, N. N.; Prosvirin, I. P.; Bukhtiyarov, A. V.; Shlyapin, D. A. Liquid-phase acetylene hydrogenation over Ag-modified Pd/Sibunit catalysts: Effect of Pd to Ag molar ratio. *Appl. Catal. a-Gen* **2020**, *600*, 117627.
- (59) Liu, F.; Xia, Y.; Xu, W.; Cao, L.; Guan, Q.; Gu, Q.; Yang, B.; Lu, J. Integration of Bimetallic Electronic Synergy with Oxide Site Isolation Improves the Selective Hydrogenation of Acetylene. *Angew. Chem., Int. Ed.* **2021**, *60*, 19324.
- (60) Komeili, S.; Ravanchi, M. T.; Taeb, A. The influence of alumina phases on the performance of the Pd-Ag/Al₂O₃ catalyst in tail-end selective hydrogenation of acetylene. *Appl. Catal. a-Gen* **2015**, *502*, 287.
- (61) Ma, Y.; Bansmann, J.; Diemant, T.; Behm, R. J. Formation, stability and CO adsorption properties of PdAg/Pd(111) surface alloys. *Surf. Sci.* **2009**, *603*, 1046.